Radial Flows in Supergranules

D. H. Hathaway
NASA/Marshall Space Flight Center, Huntsville, AL 35812

J. G. Beck
Stanford University, Stanford, CA 94305

S. Han and J. Raymond
Tennessee Technological University, Cookeville, TN 38505

Abstract. We determine the radial component of the supergranular flow velocity by examining the center-to-limb variation of the Doppler velocity signal. We acquire individual Doppler images obtained with the MDI instrument on the SOHO spacecraft and process them to remove the p-mode oscillation signal, the axisymmetric flows, the convective blueshift signal, and instrumental artifacts. The remaining Doppler signal contains only non-axisymmetric flow structures. The Doppler signal from the horizontal flows in these structures varies like $\sin\rho$, where ρ is the heliocentric angle from disk center. The Doppler signal from radial flows varies like $\cos\rho$. We fit the center-to-limb variation of the mean squared velocity signal to a straight line in $\sin^2\rho$ over the central portion of the disk. The intercept of this line at disk center gives the amplitude of the radial component of the flow. The slope of the line gives the amplitude of the horizontal component. We find that the radial flows for typical supergranules have speeds about 10% that of their associated horizontal flows or about 30 m s^{-1}. The ratio of the radial to horizontal flow speed increases from 9% to about 18% as the size of the structure decreases from > 60 Mm to ~ 5 Mm. We use data simulations to check these results and find a ratio that increases from 5% to only about 12% over the same range of sizes. These smaller ratios are attributed to an underestimation of the horizontal flow speeds due to the fact that the transverse component of the horizontal flow is not detected by Doppler measurements.

Keywords: convection, supergranules, radial flows

1. Introduction

Convective flows play several important roles in the dynamics and magnetohydrodynamics of the Sun and other stars. Their primary role is to transport heat from the deep interior to the photosphere. Their secondary roles include transporting magnetic field and angular momentum. Other important roles include the generation of the magnetic field itself through global and local magnetohydrodynamic dynamos and the generation of acoustic and MHD waves. A better understanding of these roles may be gained through improved characterizations and simulations of these convective flows. In a previous paper (Hathaway *et al.*, 2000) we examined the power spectrum of the non-axisymmetric

© 2001 *Kluwer Academic Publishers. Printed in the Netherlands.*

flows observed in the solar photosphere. We found just two principal components - granules and supergranules. This was based on a study of Doppler velocity images from the Michelson Doppler Imager (MDI) on the Solar and Heliospheric Observatory (SOHO) mission (Scherrer *et al.*, 1995). Here we study that same data to determine the characteristics of the radial flows in the supergranule component.

Supergranules were discovered in the Doppler velocity signal from the Sun by Hart (1954) but the flow was not initially associated with convection (Hart, 1956). Leighton, Noyes and Simon (1962) made that connection somewhat later based on their observations of the surface-filling cellular structure of the flow pattern. Simon and Leighton (1964) did a detailed study of the large-scale cellular flows and found that the flow velocities are predominantly horizontal with speeds of 300 - 500 m s^{-1}.

Attempts to measure the radial component of the flow in supergranulation have been hampered by the presence of both the p-mode oscillation signal and magnetic field elements. Frazier (1970) averaged together Kitt Peak magnetograph velocity data obtained 150 s apart to remove the effects of the oscillations. This revealed downdrafts with speeds of about 100 m s^{-1} associated with magnetic elements around the borders of supergranules. Similar results were found by Musman and Rust (1970) and by Deubner (1971) using different instruments and slightly different methods for removing the p-mode oscillation signal. Worden and Simon (1976) used 20 min averages of Doppler measurements taken every 48 s to reduce the p-mode oscillations. They examined the velocity signal at disk center and found downflows of $\sim$ 200 m s^{-1} in magnetic elements and upflows of $\sim$ 50 m s^{-1} in supergranule cell centers. Giovanelli (1980) used 40 min averages of measurements taken at intervals shorter than 60 s and used a data mask to exclude magnetic elements where the magnetic field strength exceeded 25 G. His disk center observations indicated radial flows with rms velocities of about 15 m s^{-1} but he estimated that residual signals due to the p-mode oscillations, unresolved granulation, and instrumental drift would contribute at the 10 m s^{-1} level. He concluded that the radial flows in supergranules have an upper limit of only 10 m s^{-1}. More recently, Wang and Zirin (1989) used 60 min averages of data obtained at 60 s intervals near disk center and found rms vertical velocities of 30 m s^{-1} in nonmagnetic areas.

The radial flows in typical granules are comparable to the horizontal flows. Beckers and Morrison (1970) observed velocities in granules and found that the radial flows were somewhat stronger than the horizontal flows observed in the Fe I 656.9 nm absorbtion line. Three-dimensional

and time-dependent numerical simulations of granulation by Nordlund (1985) and Stein and Nordlund (1998) support that conclusion.

While there is a lack of consensus on the precise amplitude of the radial flows in supergranules, it is apparent that the radial flows are much weaker than the horizontal flows. Yet, at the large wavenumber end of the spectrum, the radial flows in granules are comparable to the horizontal flows. In this paper we will examine the amplitude of the radial flows in supergranules using space-based data that is free of seeing effects along with improved techniques for isolating the velocity signals.

2. Data Preparation

We analyze Doppler velocity images acquired with the MDI instrument on SOHO. These 1024 by 1024 pixel images of the line-of-sight velocity are obtained from wavelength shifts in the Ni I 676.8 nm absorption line. Images are obtained at 60 s intervals to resolve the p-mode oscillations. We chose full-disk data from May and June of 1996 for this study. Solar activity was near its minimum during this time interval and the solar disk was devoid of active regions.

We remove the p-mode oscillation signal by averaging sequences of images with a weighted average (Hathaway, 1988a). The weighted average we employ is adapted from one used by Libbrecht and Zirin (1986). It uses 31 images and reduces the p-mode signal amplitude at 2-4 mHz by a factor of about 500. This is more than an order of magnitude improvement over simple averages as long as 60 min [see Hathaway *et al.* (2000) Figure 1]. The relative weights for the average are given by

$$w(\Delta t) = \exp[\Delta t^2/(2a^2)] - \exp[b^2/(2a^2)][1 + (b^2 - \Delta t^2)/(2a^2)] \quad (1)$$

where Δt is the time difference from the central image, $b = 16$ is the half length of the filter and $a = 8$ is the full width at half maximum all measured in minutes. This temporal filter is largely Gaussian in shape so its frequency response is also largely Gaussian. The filter is truncated at $\Delta t = \pm 16$ where both the filter weight and its first derivative vanish. This 31-minute filter reduces the p-mode signal to a level less than 1 m/s. One disadvantage of this filter is its length. Although more than 50% of the weight is on the central 9 minutes, solar rotation still introduces substantial smearing of these relatively high resolution images. We reduce this problem by "derotating" the images using the spectroscopic rotation profile of Snodgrass and Ulrich (1990).

We remove the axisymmetric flows (rotation, differential rotation, and meridional flow) and the unresolved granulation (the convective blueshift signal) using the spherical harmonic decomposition method described in Hathaway (1987) and Hathaway (1992). We find that the solar rotation signal is not well represented by a straight line from limb-to-limb at a given latitude (as it should be after the convective blueshift signal is removed). This is attributed to an error in the MDI velocity calibration and is corrected by multiplying the given velocities, V' by a function of the heliocentric angle, ρ, from disk center with the corrected velocities, V, given by

$$V(x,y) = [1 + 0.1 \sin^3 \rho] V'(x,y). \tag{2}$$

This 10% correction to the velocities is concentrated near the limb and does not influence the results of this study. The remaining signal is dominated by the non-axisymmetric flows. Typical velocities are about 300 m s^{-1} and the pattern is dominated by supergranulation. [See Hathaway *et al.* (2000) Figure 2 for an example of these data.]

We map this Doppler velocity signal, $V(x,y)$, onto heliographic coordinates (colatitude θ and longitude ϕ) and then project it onto spherical harmonics (Y_ℓ^m) such that

$$V(\theta,\phi) = \Sigma_\ell \Sigma_{m=0}^{\ell} A_\ell^m Y_\ell^m(\theta,\phi) \tag{3}$$

where the A_ℓ^m are complex amplitudes. The spherical harmonic degree, ℓ, gives the characteristic size of a component of the flow with wavelength, λ, given by

$$\lambda = \frac{2\pi R_\odot}{\ell} \approx \frac{4400}{\ell} \mathrm{Mm}. \tag{4}$$

The spherical harmonic order, m, gives the wavenumber in longitude and determines the shape of the cells for that particular spherical harmonic component.

The spectra for the convective flow components are given by the complex amplitudes for the spherical harmonic components from each image. We sample the data stream of these spectra at 60 minute intervals over 27 days from 24 May 1996 to 19 June 1996. These spectra are cleaned by removing the stationary component calculated by finding the average of the complex amplitudes for the full 27-day dataset. The signal in this stationary component contains features that remain fixed in the Doppler images including residual axisymmetric flows as well as instrumental artifacts. We then reconstruct Doppler velocity images from these cleaned spectra. The resulting velocity images are largely free of any signals due to the p-modes, the axisymmetric flows, the convective blueshift, or instrumental artifacts.

3. Radial and Horizontal Flow Components

We determine the radial and horizontal components of the flows by examining the center-to-limb variation in the Doppler velocity signal. The observed Doppler velocity consists of two components: a radial component, V_r, and a horizontal component, V_{h1}, that is directed along the line-of-sight. A second component of the horizontal flow, V_{h2}, is directed transverse to the line-of-sight and is not seen in the Doppler velocity signal. The line-of-sight Doppler velocity at each position on the disk of the Sun is given by

$$V(x,y) = V_r(x,y)\cos\rho + V_{h1}(x,y)\sin\rho, \tag{5}$$

where ρ is the heliocentric angle from disk center of the point (x,y). The mean squared line-of-sight velocity at each radial position is given by

$$\overline{V^2(\rho)} = \overline{V_r^2}\cos^2\rho + \overline{V_{h1}^2}\sin^2\rho + 2\overline{V_r V_{h1}}\cos\rho\sin\rho \tag{6}$$

where the overbars represent averages. The final term in Equation (6) should vanish since we do not expect any net correlation between the radial velocity and the line-of-sight horizontal velocity. This then gives

$$\overline{V^2(\rho)} = \overline{V_r^2} + [\overline{V_{h1}^2} - \overline{V_r^2}]\sin^2\rho \tag{7}$$

We determine typical radial and horizontal velocities by finding the mean-squared line-of-sight velocity in each of 200 annuli centered on the solar disk and then fitting these data to a linear function in $\sin^2\rho$. The intercept of this line at $\rho = 0$ gives the radial component while the slope yields the horizontal component. We analyze 20 individual cellular flow images from 20 separate days to allow solar rotation and the natural evolution of the flow pattern to produce distinctly different patterns. We fit the mean-squared line-of-sight velocity from each of these images with the linear function in Eq. 7 and determine the average and standard deviation of both $\overline{V_{h1}^2}$ and $\overline{V_r^2}$.

The results of this analysis are shown in Figure 1. The mean-squared velocity (for all 20 images) is plotted as a function of $\sin^2\rho$ along with the linear fit through the data. The linear fit gives typical horizontal velocities of 258 ± 1 m s^{-1} and typical radial velocities of 29 ± 2 m s^{-1}. Note that we only fit the data out to 60% of the distance to the limb ($\sin^2\rho = 0.36$) because foreshortening of the solar surface starts introducing curvature to the line at about that point.

We repeat this analysis with a data mask for each of the Doppler velocity images to examine possible contamination of the velocity signal by flows in magnetic elements. Although there were no active regions on the Sun at the time of the observations, the magnetic network might

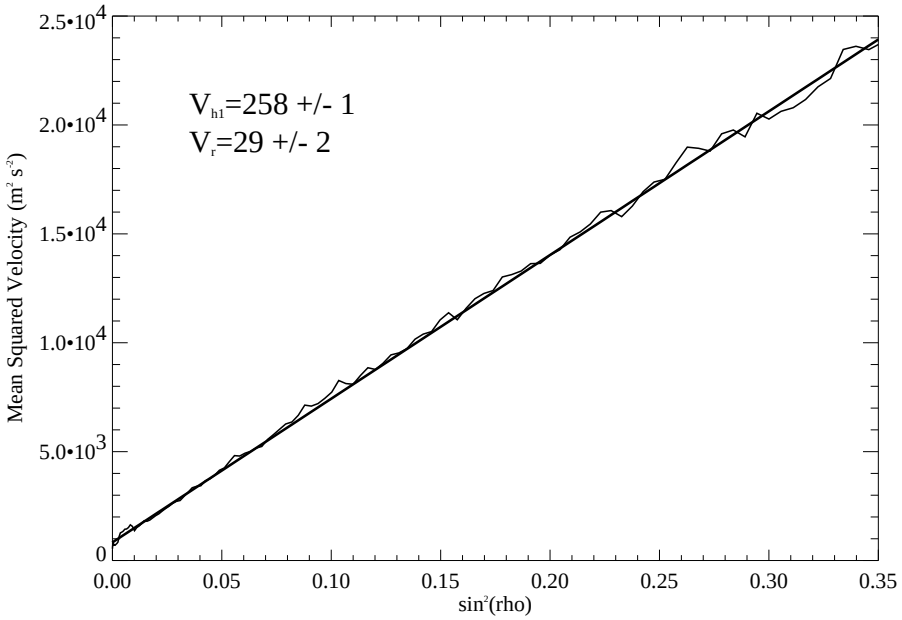

Figure 1. The mean squared velocity as a function of angular distance from disk center. The thin, ragged line represents the average from 20 individual images. The thick, straight line represents the average of the straight lines fit through each of these 20 datasets. The intercepts of these lines at $\sin^2 \rho = 0$ gives typical radial velocities of 29 ± 2 m s^{-1}. The slopes of these lines give typical horizontal velocities of 258 ± 1 m s^{-1}.

influence the velocities we observe. We construct the data masks by excluding pixels where the magnetic field strength exceeded 25 G. We identify these masked pixels using magnetograms obtained with MDI instrument during the same time interval as the Doppler images. The results indicate no contamination by magnetic elements. Although small variations in the mean-squared velocity values are seen, the final results still give the same values for the horizontal and radial flow speeds.

4. Radial Flow Component as a Function of Wavenumber

Observations and simulations of the convective flows in granules indicate that the radial flow speeds for these small cellular features are similar in magnitude to the horizontal flow speeds. This suggests that the strength of the radial flow relative to the horizontal flow should be an increasing function of wavenumber. We examine this possibility by construction images from sections of the spherical harmonic spectrum and examining the mean-squared velocity in those images.

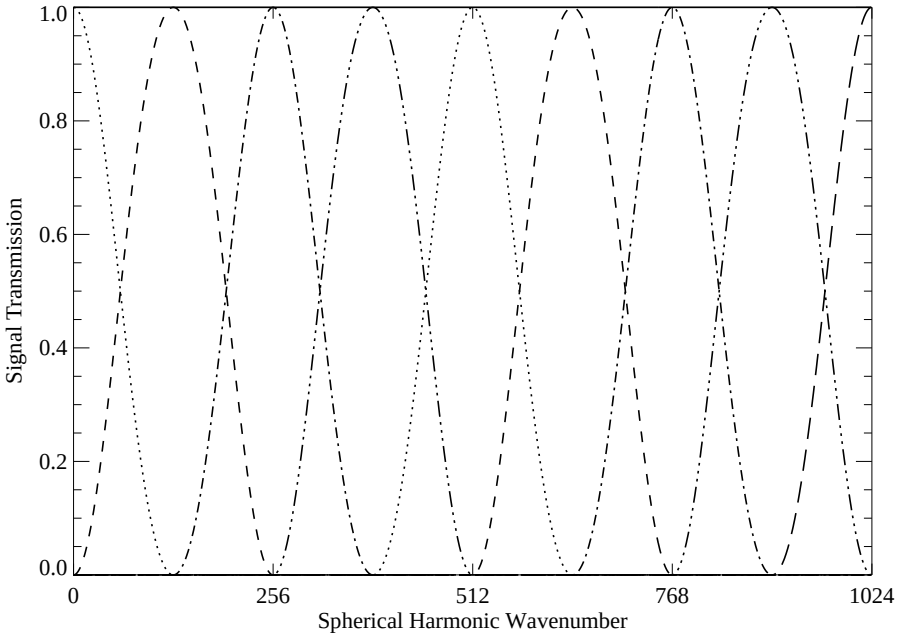

Figure 2. Spectral windows for producing a series of images containing features with increasingly larger wavenumbers. Each window has a full width of 256 wavenumbers and a full width at half maximum of 128 wavenumbers. The individual windows have centers separated by 128 wavenumbers.

We separate the spectrum from $\ell = 1$ to $\ell = 1024$ into 9 spectral bands using the Gaussian shaped window functions shown in Figure 2. We then construct images from the cleaned spherical harmonic spectra multiplied by each of these spectral windows and analyze each of these images using the method described in the previous section to determine the typical radial and horizontal flow velocities. The results of this analysis are shown in the 9 panels of Figure 3 and in tabular form in Table I. The spectral filters are identified with lower case letters (a through i). The central wavenumber for each filter is given by ℓ_c in Table I and the corresponding wavelength is λ_c. Foreshortening near the limb is not a problem for the lowest wavenumbers but it increasingly limits the useful radial range for the larger wavenumbers. The maximum distance from disk center used for the analysis of each filtered image is given in Table I by $\max(\sin\rho)$. Beyond this distance from disk center the data begin to deviate from their straight line behavior. Including these data would produce systematic errors in the fit. The goodness of fit between the data and a straight line throughout the range used in this analysis is evident in the individual panels of Figure 3. The standard errors given

in Table I are calculated from the individual fits through the filtered images for the 20 individual days.

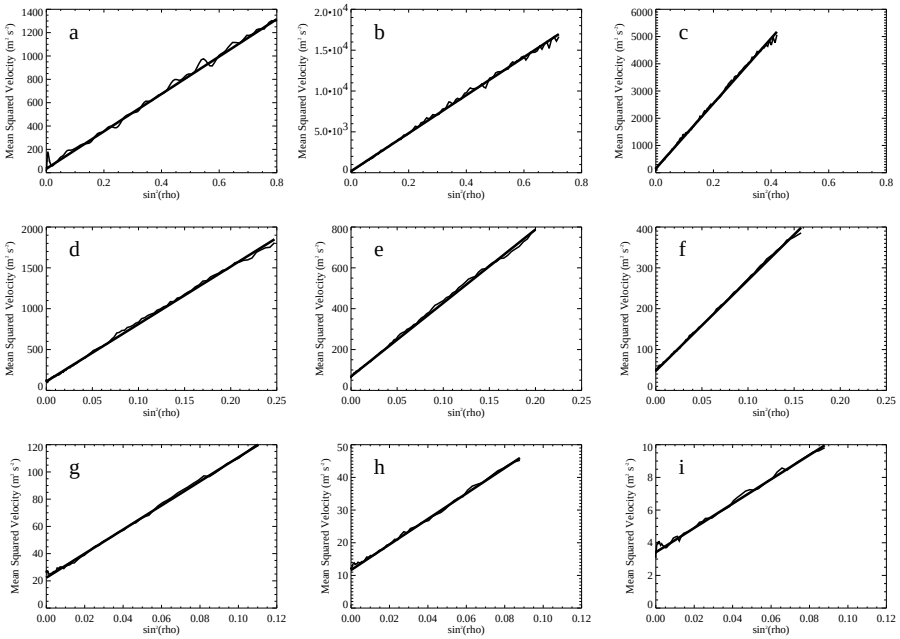

Figure 3. Mean squared velocity as functions of angular distance from disk center for the spectrally filtered images. The data for the 20 Doppler images are plotted with thin ragged lines. The best straight line fits through these data are plotted with thick straight lines. These straight line fits are excellent representations of the data and provide accurate estimates of the radial and horizontal flow speeds characteristic of each spectral band. Note that a different vertical scale is used in each of these panels.

The results we give in Table I show an increase in the strength of the radial flow speed relative to the horizontal flow speed as the wavenumber increases. At the smallest wavenumbers (largest cells) the radial flow speed is about 9% of the horizontal flow speed. At the largest wavenumbers accessible with this data ($\ell \sim 1000$) the measured radial flow speed is about 20% of the horizontal flow speed.

5. Data Simulations

We use data simulations to check these results. One problem with the analysis is that the line-of-sight velocity is completely insensitive to the transverse component of the horizontal flow. This tends to give an underestimation of the characteristic horizontal flow speed. We simulate

Table I. Horizontal and radial flow speeds for spectrally filtered data

Filter	ℓ_c	λ_c Mm	$\max(\sin\rho)$	V_h (m s^{-1})	V_r (m s^{-1})	V_r/V_h
a	0	> 60	0.90	40.5 ± 0.3	5.8 ± 1.0	0.14 ± 0.03
b	128	34	0.85	153.1 ± 0.5	13.4 ± 1.0	0.09 ± 0.01
c	256	17	0.65	110.0 ± 0.4	12.4 ± 0.5	0.11 ± 0.01
d	384	11	0.50	84.5 ± 0.5	10.4 ± 0.4	0.12 ± 0.01
e	512	9	0.45	60.5 ± 0.6	8.3 ± 0.4	0.14 ± 0.01
f	640	7	0.40	47.6 ± 0.6	6.9 ± 0.2	0.15 ± 0.01
g	768	6	0.35	30.1 ± 0.4	4.7 ± 0.1	0.16 ± 0.01
h	896	5	0.30	20.0 ± 0.3	3.4 ± 0.06	0.17 ± 0.01
i	1024	4	0.30	8.8 ± 0.2	1.85 ± 0.03	0.21 ± 0.01

the actual data by producing Doppler velocity images at 60 s intervals from an input spectrum using the method described by Hathaway (1988b).

The input spectrum uses three complex amplitudes for each spherical harmonic component to produce a vector velocity field on a spherical surface. The three amplitudes represent the amplitude of the radial flow, the amplitude of the solenoidal flow (horizontal flows with divergence), and the amplitude of the toroidal flow (horizontal flows with vorticity).

We project the vector velocity field produced from this input spectrum onto the line-of-sight to produce Doppler images. We process the Doppler images through the same temporal filtering and derotation procedures as are used on the full-disk MDI data and then analyze them with the same analysis procedures. The resulting convection spectra and center-to limb velocities are compared to those from the MDI data and the input spectrum is adjusted until a good match is obtained.

The resulting spectrum for the simulated data is shown in Figure 4. The match between the spectra is excellent throughout most of the range. The only deviations are in the details and at the extreme ends of the spectrum. The input spectrum we use to produce these results contains only two principal components - a supergranule component with peak power at a wavenumber of ~ 120 and a granule component with peak power well beyond $\ell = 1024$. This input spectrum is shown in Figure 5. Note that the granule component is only important at the highest wavenumbers.

We find a good fit with the observed center-to-limb velocity in each of the spectrally filtered images using a radial flow component that

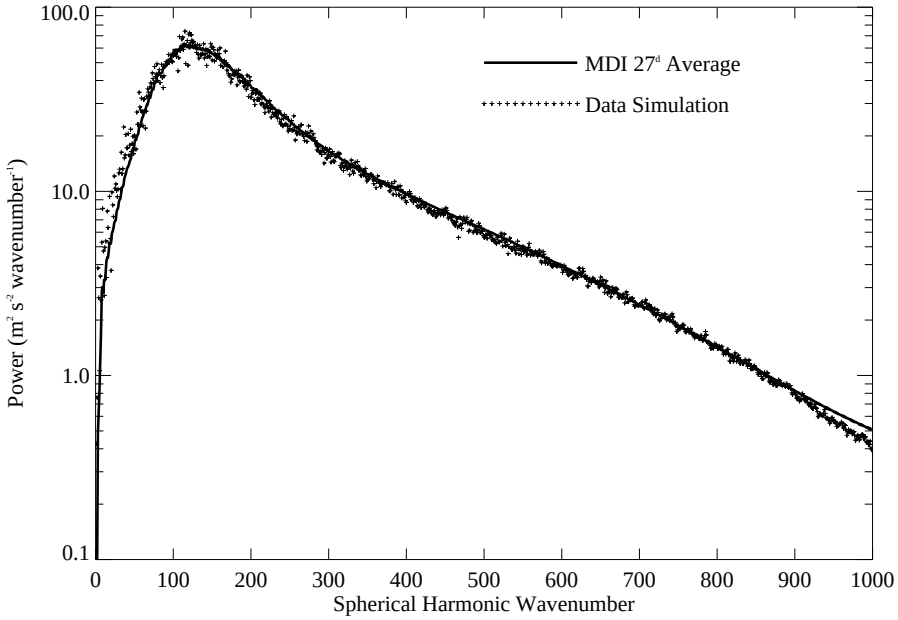

Figure 4. Power spectra for the data simulations and the MDI data. The average spectrum from the 27 days of hourly MDI Dopplergrams is shown with the solid line. An individual spectrum from the data simulations is show with the + symbols. The two spectra match very well throughout most of the range. Small deviations of a few percent in power occur at the extreme ends of the spectrum.

increases from 5% to 12% of the horizontal flow as the wavenumber increases from $\ell = 0$ to $\ell = 1000$. A simple linear function with

$$V_r = (0.05 + 0.07\ \ell/1000)V_h \tag{8}$$

is sufficient to reproduce the observed results as is shown in Figure 6.

The ratio of the radial flow speed to the horizontal flow speed is shown in Figure 6 for each of the 9 spectral bands. The match between the real data and the data simulations is excellent throughout most of the spectrum with deviations seen only at the smallest and largest wavenumbers (but still within the error estimates). The ratio used in the input spectrum for the data simulations is represented by the solid line in Figure 6. The ratios observed with both the MDI and simulated data are systematically higher by about 40%. We attribute this to an underestimation of the horizontal flows due to the unseen horizontal flow component, V_{h2}. This unseen component should be identical in size to the component we do see so we might expect the actual RMS horizontal velocity to be a factor of $\sqrt{2}$ or about 40% larger.

We show segments of the simulated data side-by-side with actual MDI data in Figure 7. It is extremely difficult to distinguish between

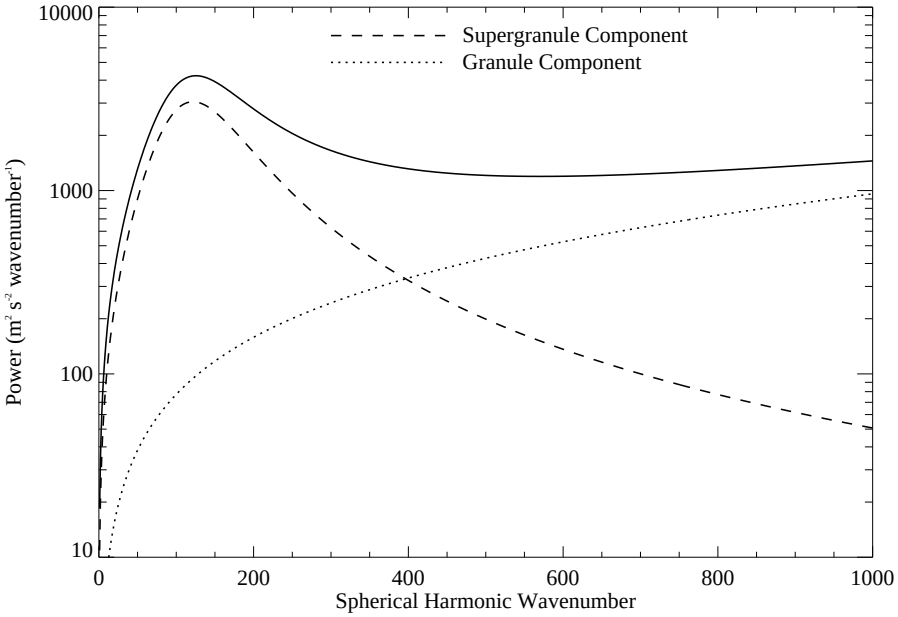

Figure 5. Input spectrum for the data simulations. Only two components are needed to produce the match seen in Figure 4. The supergranule component is given by a Lorentzian centered at $\ell \sim 120$. The granule component is given by a Lorentzian centered at $\ell \sim 4000$.

the two based on either visual inspection or statistical analysis (the power spectra in Figure 4 and the center-to-limb behavior represented in Figure 6).

6. Discussion

Since we have vector velocities for the simulated data, we base our final conclusions on the strength of the radial flow relative to the horizontal flows in these simulations. We conclude that the horizontal flow speeds determined from the Doppler data are underestimated by about 40% due to the lack of information on the transverse component of the horizontal flow. Thus, for the full spectrum of the cellular flows the RMS radial flow speed is $\sim 30 ms^{-1}$ and the RMS horizontal flow speed is $\sim 360 ms^{-1}$. This is in very close agreement with the results of Wang and Zirin (1989) but greater than the radial flow speed found by Giovanelli (1980) and less than that found by Worden and Simon (1976) and earlier authors. We have taken particular care to isolate the velocity signal due to the supergranules from that of the p-mode oscillations, axisymmetic flows, granules, and instrumental artifacts. The center-to-

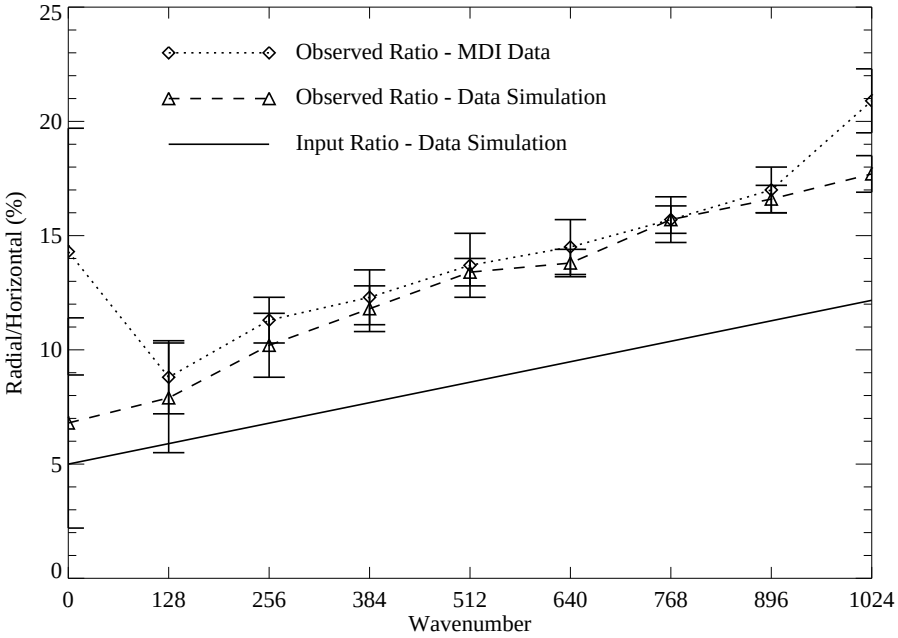

Figure 6. The ratio of the radial flow speed to the horizontal flow speed as a function of wavenumber. The ratios obtained from the MDI data agree very well with those from the data simulations. The actual ratios used as input to the data simulations are systematically smaller than the observed ratios. This is attributed to an underestimation of the horizontal flows from the line-of-sight velocity measurements.

limb behavior of the signal shown in Figure 1 gives good reason to be confident with this result. The match with the simulated data provides added support.

We have also determined the variation in the relative strength of the radial flow as a function of the size of the structures. Our direct analysis of the data gives radial flow speeds that increase from 9% of the horizontal flow speed at small wavenumbers to about 20% of the horizontal flow speeds at wavenumbers ~ 1000. Our data simulations give similar results but actually require smaller ratios with the vector velocities used to simulate the Doppler data. In the data simulations the radial flow speeds increase from 5% of the horizontal flow speeds at small wavenumbers to about 12% of the horizontal flow speeds at large wavenumbers. This variation is somewhat smaller than expected from observations of granulation where the radial flows are comparable to the horizontal flows in the photosphere at $\ell \sim 4000$.

This unexpected result may be due to the presence of the two different flow components. From our data simulation we see that supergranules dominate the spectrum from the lowest wavenumbers out to $\ell \sim 400$ (see Figure 5). The granule component doesn't start to dom-

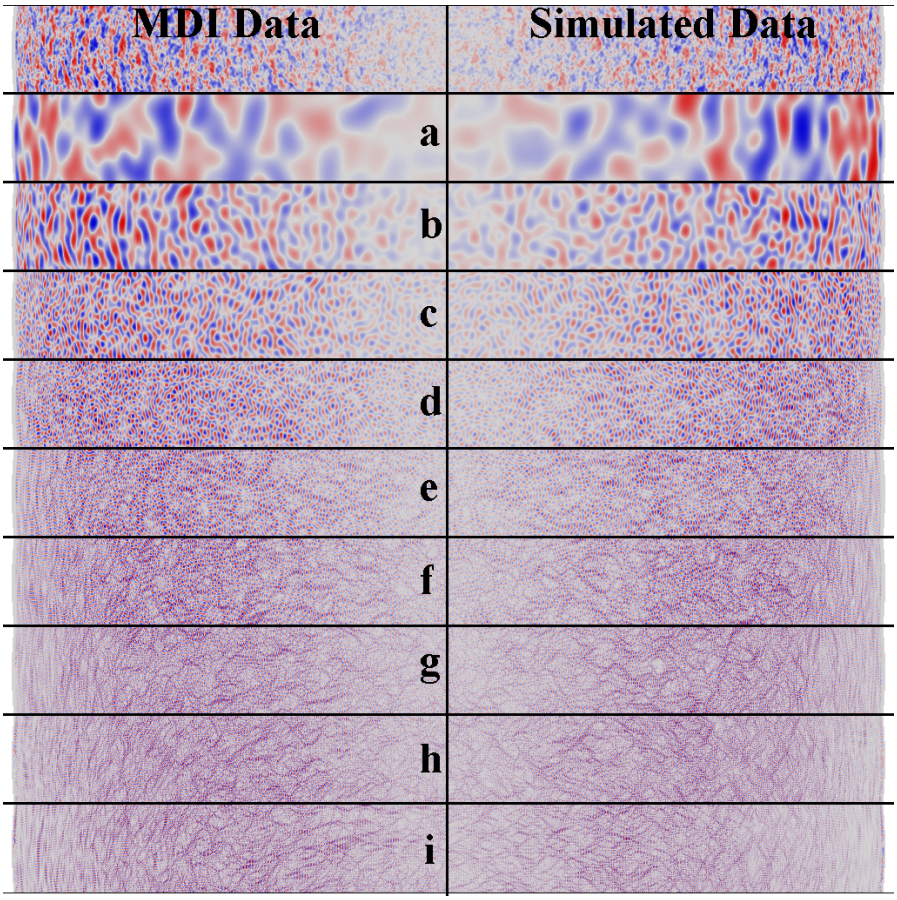

Figure 7. Comparison of MDI data (left) and simulated data (right). Segments of the Doppler images from disk center to the limb for the full cellular flows are shown at the top and each of the spectrally filtered images (a through i) are shown underneath. Red shifted areas are red, blue shifted areas are blue. The simulated data is extremely difficult to distinguish from the real data.

inate the spectrum until beyond that point and even then with much less power than at the peak. We cannot rule out the possibility that the relative strength of the radial flows increases dramatically as the granule component dominates at still higher wavenumbers. Indeed, this is probably a fair conclusion and supports the idea that the spectrum of the cellular flows has two distinctly different components.

This two component model is not without controversy. We suggest that there are two physical mechanisms that drive the cellular flows observed in the photosphere. One mechanism, thermal convection driven by the superadiabatic temperature gradient near the solar surface, drives granulation. Another mechanism drives supergranulation. The

small diffusivities for heat and momentum should allow for a very broad range of cellular flows consistent with our model spectrum. Linear stability theory suggests that cells many times wider than the depth of the layer should be produced under solar conditions. We suggest that numerical simulations of solar granulation with very broad spatial domains will indeed find broad cellular structures, albeit with low amplitude flow velocities. Other investigators do include additional flow components — mesogranules and turbulence. Lawrence, Cadavid and Ruzmaikin (1999) use wavelets to analyze Doppler velocity data and conclude that a distinct mesogranule component is needed along with a broad spectrum of turbulence. In their more recent work Lawrence, Cadavid and Ruzmaikin (2001) find interesting variations in the relative strengths of upflows and downflows as a function of wavenumber. While our technique cannot distinguish between upflows and downflows, there is no indication in Fig. 6 of any significant features in the relative strength of the radial flows as a function of wavenumber.

The radial flows we find here should lead to a corrugation of the solar photosphere with elevated regions in cell centers and depressed regions around the cell boundaries. This may, in fact, be the source of the corrugations reported recently by Kuhn *et al.* (2000). Data simulations might be used to confirm this but they will require additional information on the lifetimes and rotation rates of the cellular features.

These measurements of the radial flows in supergranules contribute to our characterization of the photospheric flows. This should lead to a better understanding of the roles these flows play in the magnetohydrodynamics of the Sun and stars. The faithful representation of the observations by our data simulations gives us hope that these simulations will prove useful in further investigations of the hydrodynamics and magnetohydrodynamics of these objects.

Acknowledgements

This work was supported by NASA's Sun-Earth Connection Enterprise through a grant from its SOHO Guest Investigator program. We acknowledge the many years of effort by the engineering and support staff of the MDI development team at the Lockheed Palo Alto Research Laboratory (now Lockheed-Martin) and the SOI development team at Stanford University. SOHO is a project of international cooperation between the European Space Agency (ESA) and NASA. We would also like to thank the referee, John Lawrence, for his useful comments and suggestions.

References

Beckers, J. M. and Morrison, R. A.: 1970, *Solar Phys.* **14**, 280.
Deubner, F.-L.: 1971, *Solar Phys.* **17**, 6.
Frazier, E. N.: 1970 *Solar Phys.* **14**, 89.
Giovanelli, R. G.: 1980 *Solar Phys.* **67**, 211.
Hart, A. B.: 1954, *Mon. Not. Roy. Astron. Soc.* **114**, 17.
Hart, A. B.: 1956, *Mon. Not. Roy. Astron. Soc.* **116**, 38.
Hathaway, D. H.: 1987, *Solar Phys.* **108**, 1.
Hathaway, D. H.: 1988a, *Solar Phys.* **117**, 1.
Hathaway, D. H.: 1988b, *Solar Phys.* **117**, 329.
Hathaway, D. H.: 1992, *Solar Phys.* **137**, 15.
Hathaway, D. H., Beck, J. G., Bogart, R. S., Bachmann, K. T., Khatri, G., Petitto, J. M., Han, S., and Raymond, J.: 2000, *Solar Phys.* **193**, 299.
Kuhn, J. R., Armstrong, J. D., Bush, R. I., and Scherrer, P.: 2000, *Nature* **405**, 544.
Lawrence, J. K., Cadavid, A. C., and Ruzmaikin, A. A.: 1999, *Astrophys. J.* **513**, 506.
Lawrence, J. K., Cadavid, A. C., and Ruzmaikin, A. A.: 2001, *Solar Phys.* in press.
Leighton, R. B., Noyes, R. W., and Simon, G. W.: 1962, *Astrophys. J.* **135**, 474.
Libbrecht, K. and Zirin, H.: 1986, *Astrophys. J.* **308**, 413.
Musman, S. and Rust, D. M.: 1970, *Solar Phys.* **13**, 261.
Nordlund, Å: 1985, *Solar Phys.* **100**, 209.
Scherrer, P. H., Bogart, R. S., Bush, R. I., Hoeksema, J. T., Kosovichev, A. G., Schou, J., Rosenberg, W., Springer, L., Tarbell, T. D., Title, A., Wolfson, C. J., Zayer, I., and the MDI Engineering Team: 1995, *Solar Phys.* **162**, 129.
Simon, G. W. and Leighton, R. B.: 1964, *Astrophys. J.* **140**, 1120.
Snodgrass, H. B. and Ulrich, R. K.: 1990, *Astrophys. J.* **351**, 309.
Stein, R. F. and Nordlund, Å.: 1998, *Astrophys. J.* **499**, 914.
Wang, H. and Zirin, H.: 1989, *Solar Phys.* **120**, 1.
Worden, S. P. and Simon, G. W.: 1976, *Solar Phys.* **46**, 73.